

# Realization of a classical Ruddlesden Popper type bilayer nickelate in $\text{Sr}_3\text{Ni}_{2-x}\text{Al}_x\text{O}_{7-\delta}$ with unusual $\text{Ni}^{4+}$

H. Yilmaz,<sup>1,\*</sup> K. Küster,<sup>2</sup> U. Starke,<sup>2</sup> O. Clemens,<sup>1</sup> M. Isobe,<sup>2</sup> and P. Puphal<sup>2,†</sup>

<sup>1</sup>University of Stuttgart, Institute for Materials Science,

Materials Synthesis Group, Heisenbergstraße 3, 70569 Germany

<sup>2</sup>Max Planck Institute for Solid State Research, Heisenbergstraße 1, 70569 Stuttgart, Germany

(Dated: June 19, 2024)

The discovery of 80 K superconductivity in bilayer  $\text{La}_3\text{Ni}_2\text{O}_7$  at pressures greater than 14 GPa presents a unique opportunity to study a novel class of high-temperature superconductors. Therefore, other bilayer nickelate following the classical ( $T^{4+}$ ) Ruddlesden-Popper (RP) series of  $\text{Sr}_3\text{Ni}_2\text{O}_7$  would present an interesting new candidate. In this work, we study the stabilization of RP  $n = 2$  phase in  $\text{Sr}_3\text{Ni}_{2-x}\text{Al}_x\text{O}_7$ , via floating zone growth of crystals. With powder and single crystal XRD, we study the stability range of the RP-type phase. Our Thermogravimetric Analysis (TGA), X-ray photoelectron spectroscopy (XPS) and gas extraction studies reveal a remarkably high oxidation state of  $\text{Ni}^{4+}$ . The obtained black crystals are insulating in transport and show a magnetic transition around 12 K.

## INTRODUCTION

The Ruddlesden-Popper (RP) series denotes structural building blocks in oxide systems consisting of alternating rocksalt and perovskite layers with the composition  $A_{n+1}T_n\text{O}_{3n+1}$ , where  $n$  is the number of consecutive perovskite blocks of  $\text{TO}_6$  octahedral layers within a structural unit. In its most common form the  $A$  site is found to be Strontium, while  $T$  are various transition metal ions both 3d and 4d (see Fig. 1 extracted from Ref. [1–10]). With this  $A = \text{Sr}$  the series denotes a clear oxidation state of  $T$  with 4+ for stoichiometric oxygen content  $\text{O}_{3n+1}$ . Due to the flexibility of the oxidation state of transition metals  $T$  a reduction down to  $\text{Sr}_3\text{T}_2\text{O}_5$  is possible for certain transition metals  $T$ . Similarly, the  $A$  site can be substituted by  $A = RE$  a rare earth ion, leading to a lower oxidation state of  $T$ . However, only for Ni a full  $A = \text{La}$  phase is reported for the whole RP phase series, which leads to a series of different oxidation states varying with  $n$ .

Nickelates have gained attention since 2019 with the discovery of superconductivity in infinite-layer nickelates [11–15], where Ni ions exhibit a formal  $3d^9$  configuration, isoelectronic and isostructural compared to cuprate superconductors [16, 17]. Even though investigations of the  $RE_{n+1}\text{Ni}_n\text{O}_{3n+1}$  compounds ( $RE = \text{rare-earth}$ ) started long ago [18–20], recent high-pressure studies reported superconductivity both in  $\text{La}_3\text{Ni}_2\text{O}_7$  [21, 22] and  $\text{La}_4\text{Ni}_3\text{O}_{10}$  [23–26] with a  $T_c$  of around 80 and 20 K, respectively. Unlike classical RP with  $T^{4+}$  Ni in  $\text{La}_3\text{Ni}_2\text{O}_7$  possesses an average  $3d^{7.5}$  configuration and  $3d^{7.33}$  in  $\text{La}_4\text{Ni}_3\text{O}_{10}$ . This is rather close to the formal  $3d^7$  state in perovskite nickelates, which were proposed to exhibit a cuprate-like electronic structure when sandwiched between layers of an insulator [27–29]. Further-

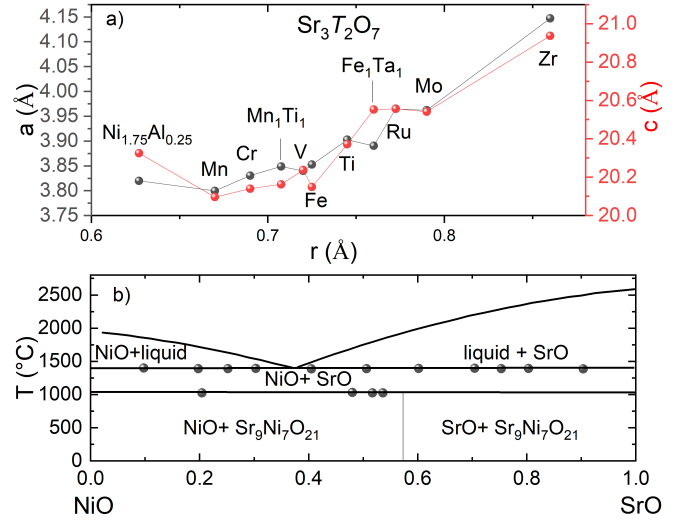


FIG. 1. **Literature status on Sr based Ruddlesden Popper nickelates.** a) Lattice constants ( $a, c$ ) versus ionic radius ( $r$ ) of the existing bilayer RP-type  $\text{Sr}_3\text{T}_2\text{O}_7$  phase with  $T =$  transition metal from Ref. [1–10], with the nickelate phase of Ref. [33]. b) Phase diagram of Sr-Ni-O (in air  $p_{\text{O}_2} = 0.209$  atm) digitized from Ref. [34].

more, an average  $3d^{7.5}$  state is reminiscent of hole-doped  $(\text{La}, \text{Sr})_2\text{NiO}_4$ , where  $3d^7$  and  $3d^8$  sites coexist [30–32].

Theoretical investigations indicate that a strong intrabilayer coupling is a key ingredient in the superconducting mechanism, but the approaches to disentangle the intermixed multiorbital states in  $\text{La}_3\text{Ni}_2\text{O}_7$  vary. Specifically, the roles assigned to low-energy Ni  $3d_{x^2-y^2}$ ,  $3d_{z^2}$ , and O  $2p$  orbital degrees of freedom diverge among the models, yielding singlet-like states with partial analogies to those of  $3d^9$  cuprates [21, 35–37] or different notions [38–48]. Notably it was found that there is polymorphism in  $\text{La}_3\text{Ni}_2\text{O}_7$  with a novel hybrid RP structure alternating of  $n = 1$  and  $n = 3$  [22]. The appearance of polymorphism limits the quality and size of the crystals

\* hasan.yilmaz@imw.uni-stuttgart.de

† puphal@fkf.mpg.de

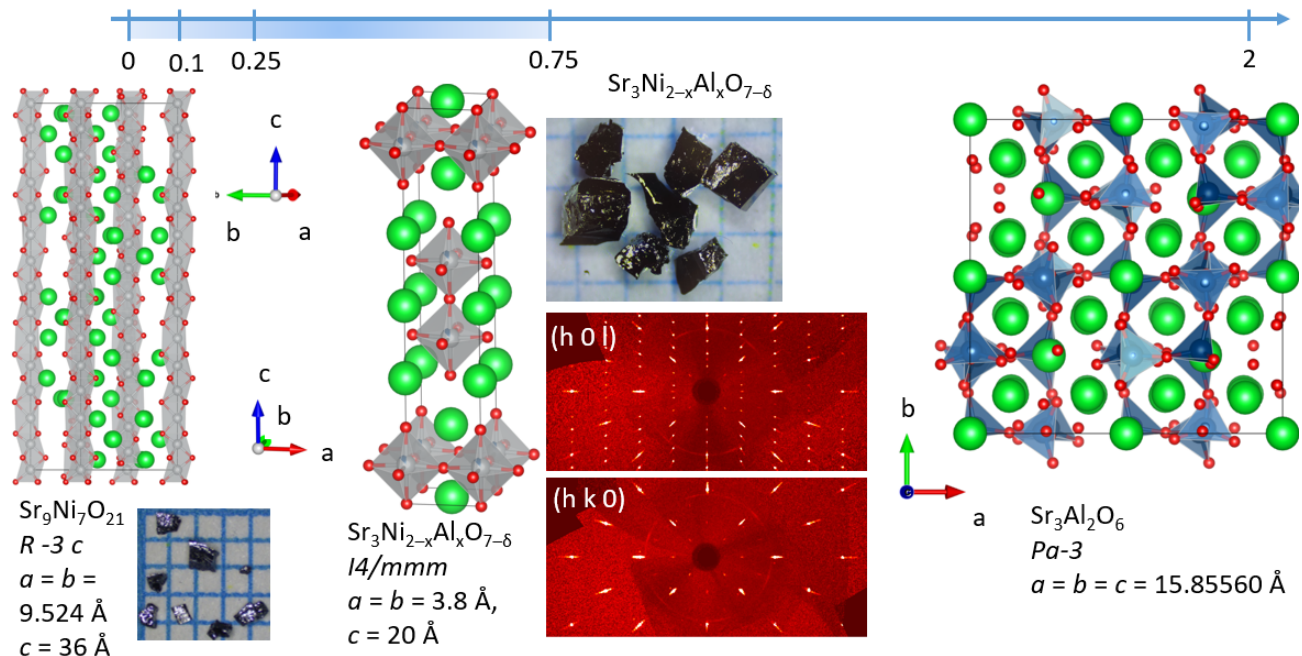


FIG. 2. **Doping dependence of the series  $\text{Sr}_3\text{Ni}_{2-x}\text{Al}_x\text{O}_7$** , following the exploration of phase formations from Optical Floating Zone (OFZ) growth at 9 bar oxygen partial pressure shown in Fig. 3. The realized structures are shown with Ni (gray), Al (blue), Sr (green), and O (red). Two pictures of crystals extracted from the boule after breaking the phases  $\text{Sr}_9\text{Ni}_7\text{O}_{21}$  (left) and  $\text{Sr}_3\text{Ni}_{2-x}\text{Al}_x\text{O}_7$  (right) are shown with a millimeter grid paper underneath. In the center below the crystal images, reconstructed maps of XRD intensities of the  $\text{Sr}_3\text{Ni}_{1.75}\text{Al}_{0.25}\text{O}_7$  single crystals are shown.

in  $\text{La}_3\text{Ni}_2\text{O}_7$  due to intergrowth of the two phases with a very narrow and close phase formation area [22]. This calls for additional RP-type nickelates to be studied in detail.

The first report on RP-type  $n = 2$  Sr-based nickelate is published in Ref. [33] based on powder samples. They found that the substitution of  $\text{Al}^{3+}$  into the Sr-Ni-O system stabilizes oxygen-deficient RP-type structures, in a stability range of  $0.5 \leq x \leq 0.75$ .

$\text{Ni}^{4+}$  is a rare oxidation state, usually found with non-distorted octahedra, as shown for  $\text{BaNiO}_3$  with a Ni-O distance of  $d = 1.8650(13) \text{ \AA}$ ,  $\text{Li}_{2-x}\text{NiO}_3$   $d = 1.88 \text{ \AA}$  [49], or  $\text{Li}_x(\text{Ni}, \text{Co}, \text{Mn})\text{O}_3$   $d = 1.9 \text{ \AA}$  [50]. Notably, both Li related compound showed that via the control of  $\text{Li}_x$ , changing the oxidation of Ni, the bond distance varied from  $\approx 2.1 \text{ \AA}$  for  $\text{Ni}^{2+}$ , to  $1.9 \text{ \AA}$  for  $\text{Ni}^{4+}$ .

In this article, we examine  $\text{Sr}_3\text{Ni}_2\text{O}_7$  single crystal formation via Al substitution, establishing a new candidate of RP-type nickelates. We confirm that the parent phase without Al does not exist as an RP-type compound even working in enhanced oxygen pressure. We find an optimal synthesized compound for  $x = 0.25$  in  $\text{Sr}_3\text{Ni}_{2-x}\text{Al}_x\text{O}_7$  in stark contrast to Ref. [33], where a minimum of  $x = 0.5$  is found. Our powder and single crystal x-ray diffraction (XRD) experiments combined with x-ray photoemission spectroscopy (XPS), thermogravimetric analysis (TGA) and gas extraction confirm an extremely rare high oxidation state of  $\text{Ni}^{4+}$ . Most importantly, these crystals form homogeneously, neither

containing impurity phases (within the resolution limits) nor showing polymorphism.

## RESULTS

### Synthesis

As shown in Fig. 1 b) the binary phase diagram of SrO-NiO taken from Ref. [34] reveals besides SrO,  $\text{Sr}_9\text{Ni}_7\text{O}_{21}$ , and NiO no RP-type phase. In accordance, for our  $x = 0$  synthesis we find no stability of a RP-type phase, but instead obtain  $\text{Sr}_9\text{Ni}_7\text{O}_{21}$  single crystals. In Tab. I structural details are summarized. However with the introduction of Aluminium on the Ni site, a RP  $n = 2$  phase emerges. In Fig. 2 we display the phases formed for varied  $x$ , where the top panel shows the  $x$  content, and below are the crystal structures shown as well as single crystal pieces. Most interestingly even the pure SrO- $\text{Al}_2\text{O}_3$  forms no RP-type phases. However, for  $x \geq 0.1$ , a mix of the RP-type phase and  $\text{Sr}_9\text{Ni}_7\text{O}_{21}$  occurs.

### Phases and structure

The corresponding XRD powder patterns of  $\text{Sr}_3\text{Ni}_{2-x}\text{Al}_x\text{O}_7$  samples are shown in Fig. 3. As can be clearly seen from Fig. 3 a), b), and c), the compounds show a high phase purity containing only

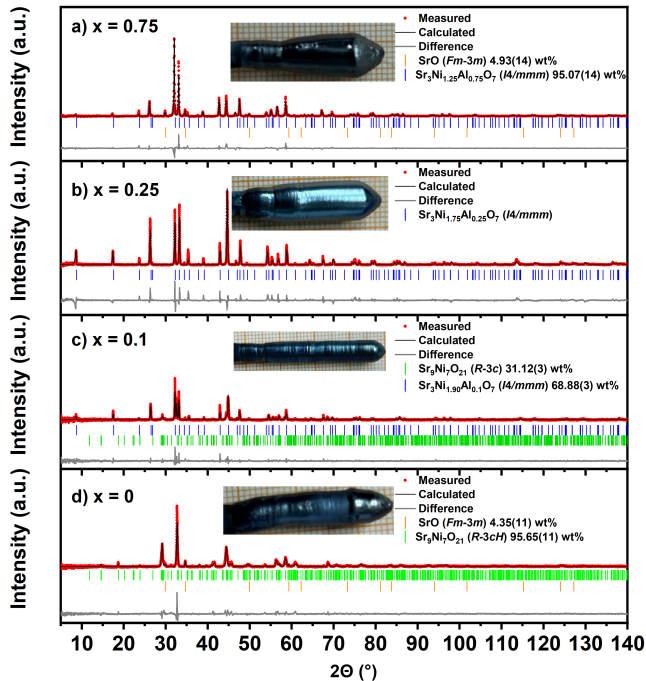


FIG. 3. Rietveld refinement of the room-temperature Powder X-ray diffraction pattern of  $\text{Sr}_3\text{Ni}_{2-x}\text{Al}_x\text{O}_7$  for a)  $x=0.75$  ; b)  $x=0.25$  c)  $x=0.10$  d)  $x=0$ . The solid black line corresponds to the calculated intensity from the Rietveld refinement, the solid gray line is the difference between the experimental and calculated intensities, and the vertical colored bars are the calculated Bragg peak positions. The underlying phases are given in the legend for phase identification of four distinct floating zone growth with pictures of the corresponding boules as an inset, with a millimeter scale underneath.

(mainly) a  $n = 2$  RP-type compound with  $I4/mmm$  (#139) symmetry. In accordance with the general RP-type  $n=2$  phase [51], Sr atoms (green) are placed in one of the large 12-coordinate sites in perovskite layers to oxygen (red) or one of the smaller 9-coordinate sites in rocksalt layers. As depicted in Fig. 2 Ni/Al (grey/blue) atoms are positioned inside anionic octahedra. The Ni-O distance of the outer oxygen amount to  $d = 1.89(3)$  Å while the inner oxygen extend to  $d = 1.984(5)$  Å and the in-plane distance lies close to outer with  $1.9038(9)$  Å. As discussed in the Introduction, compared to Li-based nickelates this shows that except for the elongated inner bond, it falls well into the expected distance for  $\text{Ni}^{4+}$  with  $1.9$  Å [49, 50]. This is quite different from the related RP  $\text{La}_3\text{Ni}_2\text{O}_7$ , which seems to show enormous distortions with the outer apical oxygen having a distance of  $2.3$  Å [21].

As mentioned above, we also investigated the undoped ( $x=0$ ) sample and Fig. 3 d) shows that it has been crystallizing  $\text{Sr}_9\text{Ni}_7\text{O}_{21}$  in the trigonal  $R-3c$  structure (see Tab. I) with 4.35% SrO impurities. As a result of this finding, we conclude that it is not possible to synthesize stoichiometric  $\text{Sr}_3\text{Ni}_2\text{O}_7$  since the oxidation state +4

TABLE I. Refined atomic coordinates of a float zone grown boule of the stoichiometry  $x=0$ : " $\text{Sr}_3\text{Ni}_2\text{O}_7$ " found to crystallize in the trigonal  $R-3c$  (#167) structure of  $\text{Sr}_9\text{Ni}_7\text{O}_{21}$ , extracted from powder XRD ( $a = 9.4527(4)$  Å,  $c = 36.004(2)$  Å,  $R_{wp} = 6.45$ ,  $GOF = 1.42$ )

Atom	Site	x	y	z	Occ
Sr	Sr01	0.3300(6)	0.3388(6)	0.69569(15)	1
Sr	Sr02	0.6766(4)	0.6766(4)	0.74431(17)	1
Ni	Ni1	1/3	2/3	2/3	1
Ni	Ni2	2/3	1/3	0.6154(6)	1
Ni	Ni3	1/3	2/3	0.7387(6)	1
Ni	Ni4	1/3	2/3	0.6869(6)	1
O	O1	0.517(2)	0.184(2)	0.6303(8)	1
O	O2	0.490(4)	0.675(3)	0.6951(10)	1
O	O3	0.499(4)	0.311(3)	0.6464(9)	1
O	O4	0.141(3)	0.667(4)	0.7549(9)	1

is not a common state for Ni and in perovskites even  $\text{Ni}^{3+}$  require enormous oxidizing conditions [52] and already for  $\text{PrNiO}_3$  with  $\text{Ni}^{3+}$  300 bar are required. The  $x = 0.10$  boule contains two phases which are 68.88%  $\text{Sr}_3\text{Ni}_{2-x}\text{Al}_x\text{O}_7$  tetragonal  $I4/mmm$  (results see Tab. II) and 31.12%  $\text{Sr}_9\text{Ni}_7\text{O}_{21}$  trigonal  $R-3c$  (depicted in Fig. 2 on the left). In contrast, the XRD analysis of a crushed crystal of  $x=0.25$  indicated a phase pure composition and also matched well with reports on powder samples with higher  $x$  [33]. The crystal structure was solved from the single-crystal XRD data, and then the determined structural model was used as a starting point for powder diffraction. The refined results are summarized in Tab. II. Unlike the powder data from literature, which suggested a stability range from 0.5 to 0.75, the  $x = 0.75$  crystal contained 4.93wt% of SrO as an impurity phase with the refinement result summarized in Tab. II, indicating a possible upper limit. The lower limit and upper limit are further discussed in the Chemical composition section. Hence, we have discovered that stabilization of the  $\text{Sr}_3\text{Ni}_2\text{O}_7$  Ruddlesden-Popper phase can be achieved by a small amount of  $\text{Al}_2\text{O}_3$  substitution. In Tab. II we list the lattice parameter versus the substitutional content which show a clear deviation for the  $a$ -axis from Vegards law below 0.25 in accordance with a separate phase evolving. We hence conclude a lower solubility limit close to 0.25.

TABLE II. Refined atomic coordinates of  $\text{Sr}_3\text{Ni}_{2-x}\text{Al}_x\text{O}_7$  in the tetragonal  $I4/mmm$  (#139) structure, extracted from powder XRD refinements shown in Fig. 3. Given are the individual  $z$  sites and occupancy (occ) for the corresponding  $x$  sorted from 0.75 to 0.25 to 0.1. The corresponding lattice constants and quality parameters are:

$x=0.75$ :  $a = 3.8126(6)$  Å,  $c = 20.3393(4)$  Å, Rwp= 5.08, GOF= 2.59;

$x=0.25$ :  $a = 3.8020(5)$  Å,  $c = 20.2616(3)$  Å, Rwp= 8.80, GOF= 2.25;

$x=0.10$ :  $a = 3.8104(6)$  Å,  $c = 20.1495(3)$  Å, Rwp= 5.82, GOF= 0.97

Atom	Site	"x = 0.75"				"x = 0.25"		"x = 0.1"	
		x	y	z	Occ	z	Occ	z	Occ
Sr	Sr01	1/2	1/2	0.8165(6)	1	0.8170(4)	1	0.8174(6)	1
Sr	Sr02	0	0	1/2	1	1/2	1	1/2	1
Ni	Ni01	1/2	1/2	0.5988(13)	5/8	0.6012(11)	7/8	0.6009(14)	19/20
Al	Al01	1/2	1/2	0.5988(13)	3/8	0.6012(11)	1/8	0.6009(14)	1/20
O	O01	1/2	1/2	0.6937(4)	1	0.6934(3)	1	0.6899(3)	1
O	O02	0	1/2	0.5922(5)	0.6333(8)	0.5911(16)	1	0.5882(3)	0.9130(7)
O	O03	1/2	1/2	1/2	1	1/2	1	1/2	1

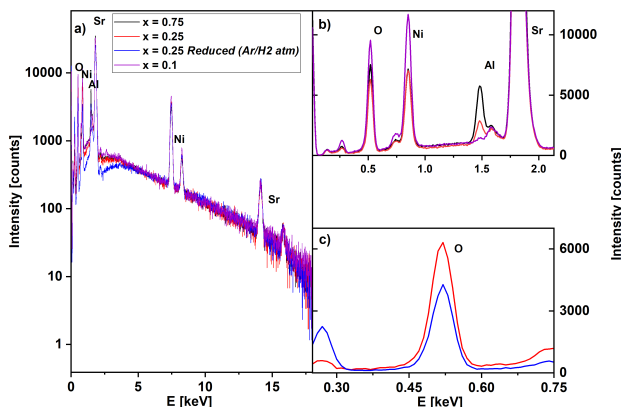


FIG. 4. **Stoichiometry:** a) Comparison of Energy-Dispersive X-ray (EDX) spectra in a logarithmic scale normalized to the Sr  $k_\beta$  line for  $x=0.75$ ,  $0.25$ ,  $0.25$  reduced, and  $0.1$  samples of the  $\text{Sr}_3\text{Ni}_{2-x}\text{Al}_x\text{O}_7$  phases. b) Magnification of the low energy part visualizing the difference in Al doping for different  $x$  (notably the given spectra of  $x = 0.1$  hints at a  $\text{Sr}_9\text{Ni}_7\text{O}_{21}$  phase). c) Magnification of the oxygen content of  $x=0.25$  for as grown (red) and reduced (blue).

### Chemical composition

We have analyzed the stoichiometry of the single crystals with a combination of energy dispersive x-ray (EDX), thermogravimetric analysis (TGA) and gas extraction. Representative EDX spectra are plotted in Fig. 4 for all compositions, as well as the reduced crystals. For the  $x = 0.75$  batch the average EDX results yield a slightly reduced Al content  $\text{Sr}_{3.02(4)}\text{Ni}_{1.38(2)}\text{Al}_{0.57(1)}\text{O}_{5.5(1)}$ , while oxygen from EDX is likely underestimated. For the  $x = 0.1$  we find as expected from the lattice parameter plot that a solubility limit is reached. Individual EDX spectra show a reduced Al content (as the one given in Fig. 4) compared to the previous batch, but this is from local points of the impurity phase  $\text{Sr}_9\text{Ni}_7\text{O}_{21}$ . This is best captured in the fact that the obtained crystals show an average stoichiometry of  $\text{Sr}_{2.99(7)}\text{Ni}_{1.75(6)}\text{Al}_{0.26(3)}\text{O}_{7(1)}$ ,

which is an equally high Al content as  $x = 0.25$ .

Finally, we focus on the optimal synthesis with  $x = 0.25$ . Here, the Al content fits very well to the expected value  $\text{Sr}_{3.03(1)}\text{Ni}_{1.81(2)}\text{Al}_{0.25(1)}\text{O}_{6.88(5)}$ . Note that only for this batch the oxygen content was determined by gas extraction as described in the methods section. We highlight the experimentally determined exact balancing of the oxygen content stabilizing  $\text{Ni}^{4+}$ , with 12.5%  $\text{Al}^{3+}$ . The annealing of this sample at 600 bar oxygen pressure did not enhance the oxygen content and none of the physical properties changed (as visible in our TGA results discussed in the following). Thus we conclude that this is the fully oxidized state.

In Fig. 5 we show the Ar-5% $\text{H}_2$  reduction of the  $x = 0.25$  variant in a TGA experiment performed at 450 °C revealing a mass loss of 5 wt% corresponding to an oxygen loss of 2 O. Resulting in a reduction towards  $\text{Sr}_3\text{Ni}_{1.75}\text{Al}_{0.25}\text{O}_5$  ( $\text{Ni}^{+1.75}$ ), which is well captured by the XRD shown in Fig. 5 c) corresponding to the formation of the orthorhombic  $Immm$   $\text{Sr}_3\text{Co}_2\text{O}_5$  type structure shown in Fig. 5 b) with the results summarized in Tab. III. The amount of decomposed parts found in powder XRD likely stems from a real reduction towards the more stable  $\text{Ni}^{2+}$  in the crystals balanced by partial decomposition. Nonetheless our EDX results on these reduced crystals yield a similar oxygen content with  $\text{Sr}_{2.98(1)}\text{Ni}_{1.81(2)}\text{Al}_{0.25(1)}\text{O}_{4.9(3)}$ , which however has to be taken with a way larger errorbar as this result stems only from EDX. Notably, with the usual separation of domains typically found in the reduction of nickelates [53, 54] we find twinned single crystals visible in the single crystal XRD maps shown on the inset of Fig. 5 a). The structural change upon reduction is clearly seen in the lattice constants (see Tab. III), where the  $c$ - and  $a$ -axis expand by 0.2 Å, while the  $b$ -axis shrinks by the same value indicating the removal of in-plane oxygen along  $b$ . This is in line with other classical  $T^{4+}$  RP, different to  $\text{La}_3\text{Ni}_2\text{O}_7$  where the  $c$ -axis shrinks by 1 Å, while  $a, b$  expand by 0.2 Å [55].

For optimally grown  $\text{Sr}_3\text{Ni}_{1.75}\text{Al}_{0.25}\text{O}_7$  we have in addition performed XPS measurements to confirm the unusual  $\text{Ni}^{4+}$  state. In Fig. 6 we show the Ni 2p and Sr 3d

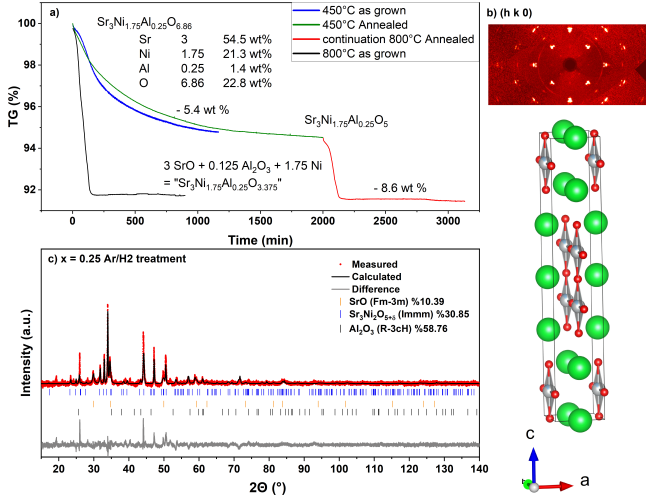


FIG. 5. **Topochemical oxygen reduction realized via a)** Thermogravimetric analysis (TGA) of the  $\text{Sr}_3\text{Ni}_{1.75}\text{Al}_{0.25}\text{O}_7$  ( $x=0.25$ ) single crystals both annealed and not annealed heated at  $450^\circ\text{C}$  and  $800^\circ\text{C}$  in Ar/5% $\text{H}_2$  flow plotted versus time. **b)** Crystal structure derived from XRD are shown with Ni(grey), Al (blue), Sr (green) and O (red). **c)** Rietveld refinement of the room-temperature XRD pattern of  $\text{Sr}_3\text{Ni}_{1.75}\text{Al}_{0.25}\text{O}_7$  crushed single crystals after Ar/ $\text{H}_2$  treatment. The solid black line corresponds to the calculated intensity from the Rietveld refinement, the solid gray line is the difference between the experimental and calculated intensities, and the vertical colored bars are the calculated Bragg peak positions with the phases written in the legend.

TABLE III. Refined atomic coordinates of Ar/ $\text{H}_2$  treated  $\text{Sr}_3\text{Ni}_{1.75}\text{Al}_{0.25}\text{O}_{7-\delta}$  found to crystallize in the orthorhombic  $Immm$  (#71) structure, extracted from powder XRD ( $a = 3.603(2)$  Å,  $b = 3.839(3)$  Å,  $c = 20.442(14)$  Å; Rwp= 7.00, GOF= 0.95)

Atom	Label	x	y	z	Occ
Sr	Sr1	1/2	1	0.1780(4)	1
Sr	Sr2	0	1/2	1/2	1
Ni	Ni1	1/2	1	0.3996(8)	7/8
Al	Al1	1/2	1	0.3996(8)	1/8
O	O1	1/2	1	0.3150(3)	0.5415(7)
O	O2	1/2	1	1/2	1
O	O3	1/2	1/2	3677(14)	1

spectra, and compare it to literature results of comparable  $\text{Ni}^{3+}$  and  $\text{Ni}^{4+}$ , which reveal that for our crystals we find a mixture of the two oxidation states. The strongest peak is at  $855.6$  eV originating from  $\text{Ni}^{4+}$ , with a shoulder at  $854$  eV. This shoulder is more intense compared to the one in  $\text{Li}_2\text{NiO}_3$ . Since it is at a similar binding energy to the main peak in  $\text{LaNiO}_3$  where Ni is in 3+ oxidation state we conclude that there is a small amount of  $\text{Ni}^{3+}$  in our  $\text{Sr}_3\text{Ni}_{1.75}\text{Al}_{0.25}\text{O}_7$ . Sr 3d shows two doublets one with the Sr  $3d_{5/2}$  binding energy at  $131.5$  eV and a second one at  $133.5$  eV. The latter can be related to the instability of Sr on the surface probably reacting to

Sr-oxide or hydroxide [56].

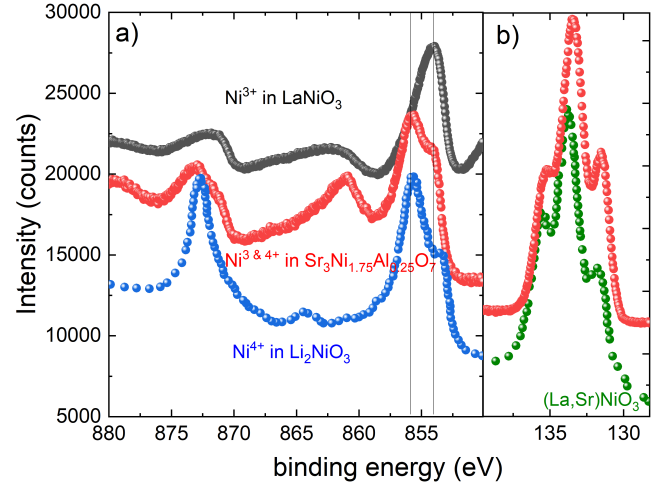


FIG. 6. **X-ray Photoemission Spectroscopy (XPS)** of Ni 2p and Sr 3d in  $\text{Sr}_3\text{Ni}_{1.75}\text{Al}_{0.25}\text{O}_7$  compared to a XAS spectra of  $\text{Li}_2\text{NiO}_3$  [49] and our XPS of  $\text{LaNiO}_3$ , as well as Sr doped  $\text{LaNiO}_3$  [52].

### Magnetic and electrical properties

Finally, we investigate the physical properties of this classical RP-type nickelate phase. First we consider the spin state of  $\text{Ni}^{4+}$ . The low spin configuration has  $t_{2g}^0 e_g^6$ ,  $S = 0$  resulting in a nonmagnetic ion, while the high spin

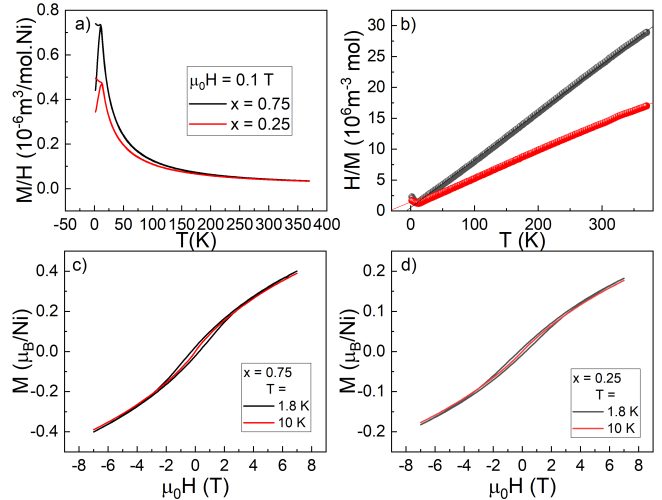


FIG. 7. **Doping dependence of the magnetism.** a) Magnetization versus temperature of a  $\text{Sr}_3\text{Ni}_{1.25}\text{Al}_{0.75}\text{O}_7$  ( $x=0.75$ ) and a  $\text{Sr}_3\text{Ni}_{1.75}\text{Al}_{0.25}\text{O}_7$  ( $x=0.25$ ) single crystals showing a magnetic transition at  $11.5$  K and  $12.5$  K. b) Inverse of the magnetization versus temperature with a Curie-Weiss fit. Magnetization versus field of c)  $\text{Sr}_3\text{Ni}_{1.25}\text{Al}_{0.75}\text{O}_7$  ( $x=0.75$ ) and d)  $\text{Sr}_3\text{Ni}_{1.75}\text{Al}_{0.25}\text{O}_7$  ( $x=0.25$ ) at  $1.8$  and  $10$  K.

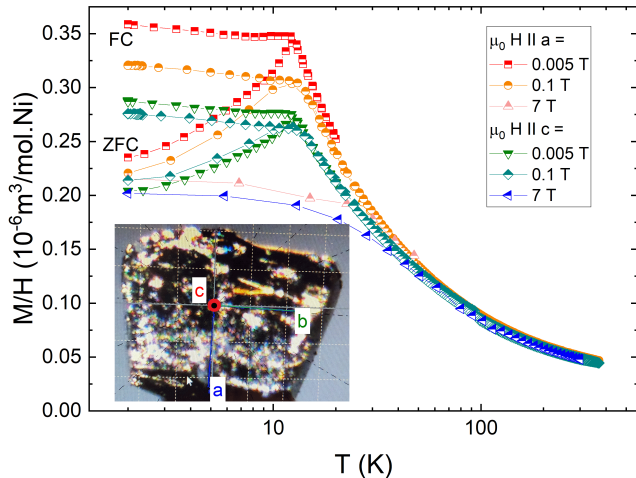


FIG. 8. **Anisotropy** and field dependence of the Magnetization versus temperature on a logarithmic scale to focus on the low temperature transition of a  $\text{Sr}_3\text{Ni}_{1.75}\text{Al}_{0.25}\text{O}_7$  ( $x=0.25$ ) single crystal in zero-field cooled (ZFC) and field cooled (FC) manner in fields of 0.005, 0.1 and 7 T.

state would have  $t_{2g}^2 e_g^4$ ,  $S = 2$ .

As discussed in the XRD section the inner Ni-O distance is extended to 1.984(4) Å, while the others lie around the expected 1.9 Å. The elongation of the inner oxygen bond hints at an energy lowering of z-axis-based energy levels and a high spin state. Notably as discussed in Ref. [57], a dynamic Jahn-Teller effect is provided by the spectra of impurities belonging to the iron group, which occupy interstitial positions. Here, g-factors for  $3d^6$  vary from 3 to 3.4 resulting in a reduction of the effective moment. Due to the site-mixed nature of our nickelates, this scenario might play a role.

Our magnetic susceptibility measurements are displayed in Fig. 7. Over all Al dopings the crystals reveal a magnetic transition at around 12 K, which subtly shifts with  $x$ . Curie-Weiß fits show a  $\theta_W = -8$  and  $-50$  K with a  $\mu_{eff} = 2.9\mu_B$  and  $3.87\mu_B$  for  $x = 0.75$  and  $x = 0.25$  closer to the expected moment of  $\text{Ni}^{3+}$  with  $\mu_{eff} = 3.9\mu_B$ , while  $\text{Ni}^{4+}$  high spin has an effective moment of  $\mu_{eff} = 4.9\mu_B$  (note, however, the possibility of a reduced g-factor). The Magnetization versus field of both  $x = 0.75$  and  $x = 0.25$  show a hysteresis at 1.8 K with a coercive field around 0.25 T, a remnance of  $0.011\mu_B$ , but even at 7 T the magnetization is far from saturation, indicating stronger exchange interactions than given from the Curie-Weiß fit.

To investigate the field dependence and magnetic anisotropy we carefully checked a crystal by single crystal XRD and oriented it in this process. In Fig. 8 we see no major anisotropy concluding a spin-glass transition that is slowly suppressed by external fields and obviously originates from nonmagnetic Al site vacancies.

As the magnetic properties of the trigonal phase  $\text{Sr}_9\text{Ni}_7\text{O}_{21}$  are yet unexplored, we performed a magne-

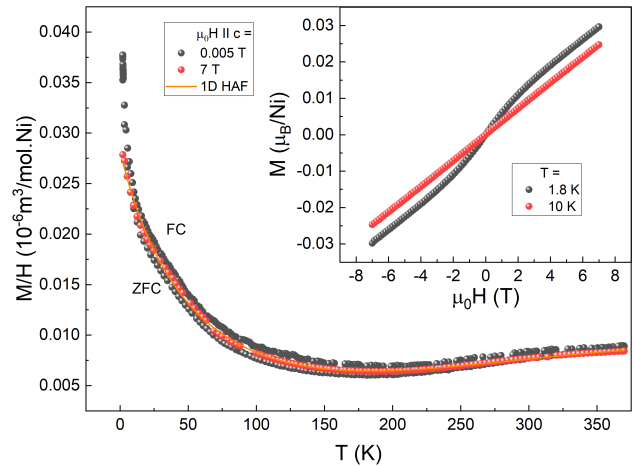


FIG. 9.  $\text{Sr}_9\text{Ni}_7\text{O}_{21}$  Magnetization versus temperature of a  $\text{Sr}_9\text{Ni}_7\text{O}_{21}$  single crystals in a field of 0.005 T and 7 T. The inset shows the magnetization versus field at 1.8 and 10 K.

tization measurement of our rather inhomogenous crystals grown from off-stoichiometry, which however only contains nonmagnetic impurities. Notably from the stoichiometry we expect Ni close to  $3+$ , likely in the high spin state  $t_{2g}^5 e_g^2$ ,  $S = 3/2$  and  $J = 9/2$ . Looking at the structure shown in Fig. 2, we find NiO face sharing chains, likely realizing a low dimensional quantum magnet indicated by a maximum seen in the susceptibility in Fig. 9. Commonly found for  $\text{Ni}^{3+}$  an effective  $S = 1/2$  state is realized (e.g.  $\text{RNiO}_3$ ) this would allow us to describe our susceptibility versus temperature with a one dimensional Heisenberg Antiferromagnetic Chain (1D HAF) in addition with a curie term. Such a fit would result in an exchange coupling of 803(30) K. This likely overestimates  $J$ , which however certainly lies above our highest accessed temperature, i.e. 370 K. We observe a subtle zero-field cooled bifurcation indicating glassiness from structural disorder, and derivatives of the susceptibility show no transitions down to 2 K. The magnetization versus field at 10 K is linear, whereas the lowest temperature one shows a subtle kink around 1.4 K, likely from saturation of the paramagnetic contribution. Overall, the moment is small and far from saturation.

$\text{Sr}_9\text{Ni}_7\text{O}_{21}$  forms black crystals that are insulating. A quick four-point resistivity measurement failed as the resistance is above  $\text{G}\Omega$ . In Fig. 10 we show the resistivity of a  $x = 0.25$  crystal, which reveals insulating behaviour likely induced by the Al doping. An estimation of the band gap energy via an Arrhenius law is applied at high temperatures. Here, all carriers are thermally excited across the band gap, and hence the electron and hole concentrations are equal. The fit yields  $E_g = 1250$  K using  $\rho = \rho_0 \exp(E_g/(kT))$ . Notably, all crystals are black, so future doping, or Al alternatives, might allow for the establishment of a metallic bilayer RP-type phase.

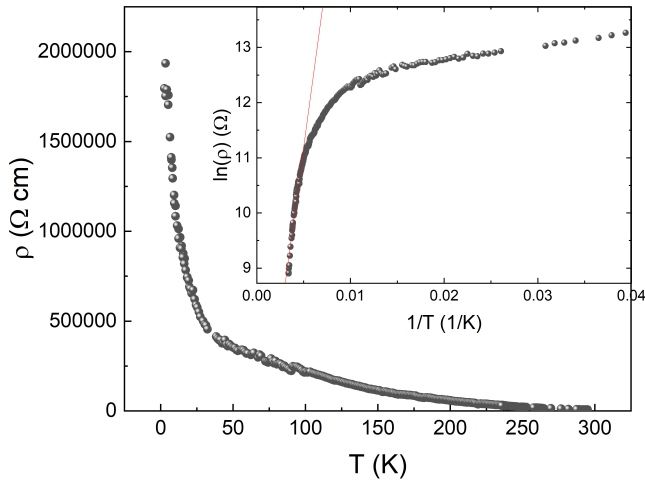


FIG. 10. **Electrical transport** versus temperature of  $\text{Sr}_3\text{Ni}_{1.75}\text{Al}_{0.25}\text{O}_7$  showing highly insulating behaviour. The inset shows an Arrhenius plot.

## DISCUSSION

In Summary, we have presented the stabilization of bilayer  $n=2$  Ruddlesden-Poppers type Nickelate  $\text{Sr}_3\text{Ni}_2\text{O}_7$  via Al substitution on the Ni site, with the classical ( $T^{4+}$ ) RP-type  $n = 2$  tetragonal  $I4/mmm$  structure. With  $\text{Sr}_3\text{Ni}_{1.75}\text{Al}_{0.25}\text{O}_7$  we find the optimal stoichiometry in terms of phase purity and crystallinity, where unlike  $\text{La}_3\text{Ni}_2\text{O}_7$  no polymorphism and a wide phase stability range are observed. The oxygen content is determined to exactly balance the  $\text{Al}^{3+}$  content with the formation of stable  $\text{Ni}^{4+}$  using two independent techniques that lead to the final composition  $\text{Sr}_3\text{Ni}_{1.75}\text{Al}_{0.25}\text{O}_{6.88}$ . In particular, this is the fully oxidized sample, and no orthorhombic transition occurs even with annealing at 600 bar, in contrast to  $\text{La}_3\text{Ni}_2\text{O}_7$ . After reduction the system becomes orthorhombic  $Immm$   $\text{Sr}_3\text{Ni}_{1.75}\text{Al}_{0.25}\text{O}_{5.125}$  with stable  $\text{Ni}^{2+}$ . Notably, the stabilization of  $\text{Ni}^{4+}$  via Al substitution could help in Li-Ni-based battery applications and shows an enormous potential for stabilization of metastable phases. Our transport measurements show that the black crystals are insulating. We encourage theoretical calculations on the unique stabilization via  $\text{Al}^{3+}$ , while a try of  $\text{Ti}^{4+}$  (not shown) instead resulted in the formation of a  $n = 1$  RP-type phase, and Al free synthesis gave crystals of the trigonal  $\text{Sr}_9\text{Ni}_7\text{O}_{21}$  realizing face sharing one dimensional chains. Hence, theoretical predictions of an optimal B site cation are desired. Although the crystals are insulating pressurization might enhance metallicity in these black crystals, as was shown for the insulating  $\text{La}_3\text{Ni}_2\text{O}_6$  with the same crystal structure [55]. Moreover, chemical doping will be pursued in the near future giving hope to novel nickelate superconductors.

## METHODS

### Synthesis

For the synthesis of  $\text{Sr}_3\text{Ni}_{1.75}\text{Al}_{0.25}\text{O}_7$  single crystals we utilize the optical floating zone (OFZ) technique under 9 bar oxygen partial pressure. First, the feed rods were prepared by conventional Solid-State methods using stoichiometric amounts of  $\text{SrCO}_3$  (Sigma Aldrich, 99.995%),  $\text{NiO}$  (Alfa Aesar, 99.998%) and  $\text{Al}_2\text{O}_3$  (Alfa Aesar, 99.995%). The precursor powders were mixed using a ball mill and sintered in an aluminum oxide crucible at 1200 °C for 12 hours in air. The as-sintered powders were pressed into cylindrical rods ( $\phi = 4$  mm,  $l = 100$  mm) by an isostatic press (70 Mpa) using rubber forms and subsequently annealed at 1200 °C 12 hours in air. The rods were then installed in an Optical Float Zone Furnace (FZ-T-10000-H-III-VPR). Finally, single crystal growth was conducted equipped with 4x1000 W- halogen lamps. During the growth process, feed and seed rods were counter-rotated (24 rpm) in order to minimize the diffusion zone close to the crystallization surface. Oxygen gas flow (100 cc/min) was applied and an auxiliary pressure of 9 bar was introduced simultaneously for forming the oxidized phase. To obtain relatively large single crystals, the growth rate was stabilized to 4 mm/h with feeding at the same rate. Post-growth, the boule was cracked using a mortar and single crystals were selected for further analysis. Selected crystals have been annealed using a high pressure gas autoclave with a gold membrane compressor at 600 bar oxygen pressure and 600°C for 4 days.

### Diffraction

The crystallinity and phase purity of the as-grown single crystals were checked using XRD on powdered samples. Powder XRD measurements were performed on ground crystals in order to examine the presence of impurity as well as to determine the crystal structure and lattice parameters. XRD patterns were recorded at room temperature using a Rigaku Miniflex diffractometer with Bragg-Brentano geometry,  $\text{Cu K}_\alpha$  radiation and a Ni filter. Rietveld refinements were conducted with the TOPAS V6 software. Single-crystal diffraction was performed at room temperature using a Rigaku XtaLAB mini II instrument with  $\text{Mo K}_\alpha$  radiation. The data was analyzed with CrysAlis(Pro) and the final refinement was done using Olex2 with SHELX.

### Chemical composition

XPS data were collected using a commercial Kratos AXIS Ultra spectrometer and a monochromatized  $\text{Al K}_\alpha$  source (photon energy, 1486.6 eV). The spectra were collected using an analyzer with a pass energy of 20 eV. Due

to the insulating nature of the sample a charge neutralizer was used and the C 1s was set to 284.8 eV (adventitious carbon) for binding energy calibration [58]. XPS spectra were analyzed using the CASAXPS software. All samples were cleaved in a glove box, mounted via silver paint on a pin, and transported under an inert atmosphere to the XPS chamber. Energy-dispersive x-ray spectra (EDX) were recorded with a NORAN System 7 (NSS212E) detector in a Tescan Vega (TS-5130MM) Scanning electron microscope (SEM). Differential Thermal Analysis studies (DTA) and Thermo gravimetry (TG) was done using a Netzsch DTA/TG. Via an Eltra ONH-2000 analyzer we determine the precise oxygen content, where the samples were placed in a Ni crucible, clipped and heated. A carrier gas takes the oxygen, after which the oxygen reacts with carbon and CO<sub>2</sub> is detected in an infrared-cell. Each measurement is repeated three times and compared with a standard. The quoted error bars give the statistical error.

### Magnetic and electric properties

Magnetic susceptibility measurements were performed using a vibrating sample magnetometer (MPMS 3, Quan-

tum Design). Electrical transport measurements were carried out with a Physical Property Measurement System (PPMS, Quantum Design).

### AUTHOR CONTRIBUTIONS

P.P. conceived the project supervised the experiments and measured transport and magnetization. H.Y. grew the crystals, performed XRD measurements under the supervision of P.P.. O.C. and M.I. were responsible for the project management. XPS samples were prepared by P.P., measured and analyzed by K.K. and U.S.. H.Y. and P.P. wrote the manuscript with comments from all authors.

### ACKNOWLEDGMENTS

We thank Samir Hammoud for carrying out gas extraction studies. Part of the magnetic measurements are based on a VSM-SQUID of the solid state spectroscopy department at Max Planck Institute for Solid State Research, Heisenbergstrasse 1, 70569 Stuttgart, Germany.

- 
- [1] J. Mitchell, J. Millburn, M. Medarde, S. Short, J. Jorgensen, and M. Fernandez-Diaz, Sr<sub>3</sub>Mn<sub>2</sub>O<sub>7</sub>: Mn<sup>4+</sup> parent compound of the n=2 layered cmr manganites, *Journal of Solid State Chemistry* **141**, 599 (1998).
- [2] E. Castillo-Martinez and M. A. Alario-Franco, Revisiting the sr-cr(iv)-o system at high pressure and temperature with special reference to Sr<sub>3</sub>Cr<sub>2</sub>O<sub>7</sub>, *Solid State Sciences* **9**, 564 (2007).
- [3] I. B. Sharma, C. Singh, and D. Singh, Synthesis, structure, electric transport and magnetic properties of Sr<sub>3</sub>MnTiO<sub>7-δ</sub>, *Journal of Alloys and Compounds* **375**, 11 (2004).
- [4] M. Itoh, M. Shikano, H. Kawaji, and T. Nakamura, Structural aspects on the variations of electric and magnetic properties of the layered compound system Sr<sub>n+1</sub>V<sub>n</sub>O<sub>3n+1-δ</sub> (n = 1, 2, 3 ∞), *Solid State Communications* **80**, 545 (1991).
- [5] S. Dann, M. Weller, and D. Currie, Structure and oxygen stoichiometry in Sr<sub>3</sub>Fe<sub>2</sub>O<sub>7-y</sub> 0 ≤ y ≤ 1.0, *Journal of Solid State Chemistry* **97**, 179 (1992).
- [6] M. M. Elcombe, E. H. Kisi, K. D. Hawkins, T. J. White, P. Goodman, and S. Matheson, Structure determinations for Ca<sub>3</sub>Ti<sub>2</sub>O<sub>7</sub>, Ca<sub>4</sub>Ti<sub>3</sub>O<sub>10</sub>, Ca<sub>3.6</sub>Sr<sub>0.4</sub>Ti<sub>3</sub>O<sub>10</sub> and a refinement of Sr<sub>3</sub>Ti<sub>2</sub>O<sub>7</sub>, *Acta Crystallographica Section B Structural Science* **47**, 305 (1991).
- [7] H. Müller-Buschbaum and J. Wilkens, Ein Beitrag über Sr<sub>2</sub>RuO<sub>4</sub> und Sr<sub>3</sub>Ru<sub>2</sub>O<sub>7</sub> zur oktaederstreckung von M<sup>4+</sup> in K<sub>2</sub>NiF<sub>4</sub>- und Sr<sub>3</sub>Ti<sub>2</sub>O<sub>7</sub>-typ-verbindungen, *Zeitschrift für anorganische und allgemeine Chemie* **591**, 161 (1990).
- [8] Z. Li, G. Li, J. Sun, Y. Wang, L. You, and J. Lin, Structural and magnetic properties of ruddlesden-popper compounds in a double-perovskite family Sr<sub>n</sub>(Fe, Ta)<sub>n</sub>O<sub>3n</sub>(SrO), *Solid State Sciences* **8**, 1035 (2006).
- [9] Q. Li, J. Si, T. Duan, X. Zhu, and H.-H. Wen, Synthesis, structure, and physical properties of bilayer molybdate Sr<sub>3</sub>Mo<sub>2</sub>O<sub>7</sub> with flat-band, *Philosophical Magazine* **100**, 2402 (2020).
- [10] I. Fukasawa, Y. Maruyama, S. Yoshida, K. Fujita, H. Takahashi, M. Ohgaki, M. Nagao, S. Watauchi, V. Gopalan, K. Tanaka, and I. Tanaka, Growth and phase transition of Sr<sub>3</sub>Zr<sub>2</sub>O<sub>7</sub> single crystals, *Journal of Crystal Growth* **615**, 127241 (2023).
- [11] D. Li, K. Lee, B. Y. Wang, M. Osada, S. Crossley, H. R. Lee, Y. Cui, Y. Hikita, and H. Y. Hwang, Superconductivity in an infinite-layer nickelate, *Nature* **572**, 624 (2019).
- [12] Y. Nomura and R. Arita, Superconductivity in infinite-layer nickelates, *Rep. Prog. Phys.* **85**, 052501 (2022).
- [13] M. Hepting, M. P. M. Dean, and W.-S. Lee, Soft X-Ray Spectroscopy of Low-Valence Nickelates, *Front. Phys.* **9**:808683 (2021).
- [14] H. Chen, A. Hampel, J. Karp, F. Lechermann, and A. J. Millis, Dynamical Mean Field Studies of Infinite Layer Nickelates: Physics Results and Methodological Implications, *Front. Phys.* **10**:835942 (2022).
- [15] K. Held, L. Si, P. Worm, O. Janson, R. Arita, Z. Zhong, J. M. Tomczak, and M. Kitatani, Phase Diagram of Nickelate Superconductors Calculated by Dynamical Vertex Approximation, *Front. Phys.* **9**:810394 (2022).
- [16] B. Keimer, S. A. Kivelson, M. R. Norman, S. Uchida, and J. Zaanen, From quantum matter to high-temperature superconductivity in copper oxides, *Nature* **518**, 179 (2015).

- [17] P. A. Lee, N. Nagaosa, and X.-G. Wen, Doping a mott insulator: Physics of high-temperature superconductivity, *Rev. Mod. Phys.* **78**, 17 (2006).
- [18] M. Greenblatt, Ruddlesden-Popper  $\text{Ln}_{n+1}\text{Ni}_n\text{O}_{3n+1}$  nickelates: structure and properties, *Curr. Opin. Solid State Mater. Sci.* **2**, 174 (1997).
- [19] J. Rodriguez-Carvajal, M. T. Fernandez-Diaz, and J. L. Martinez, Neutron diffraction study on structural and magnetic properties of  $\text{La}_2\text{NiO}_4$ , *J. Phys.: Condens. Matter* **3**, 3215 (1991).
- [20] J. B. Torrance, P. Lacorre, A. I. Nazzari, E. J. Ansaldo, and C. Niedermayer, Systematic study of insulator-metal transitions in perovskites  $\text{RNiO}_3$  ( $R = \text{Pr, Nd, Sm, Eu}$ ) due to closing of charge-transfer gap, *Phys. Rev. B* **45**, 8209 (1992).
- [21] H. Sun, M. Huo, X. Hu, J. Li, Z. Liu, Y. Han, L. Tang, Z. Mao, P. Yang, B. Wang, J. Cheng, D.-X. Yao, G.-M. Zhang, and M. Wang, Signatures of superconductivity near 80 K in a nickelate under high pressure, *Nature* **621**, 493–498 (2023).
- [22] P. Puphal, P. Reiss, N. Enderlein, Y.-M. Wu, G. Khalilullin, V. Sundaramurthy, T. Priessnitz, M. Knauft, L. Richter, M. Isobe, P. A. van Aken, H. Takagi, B. Keimer, Y. E. Suyolcu, B. Wehinger, P. Hansmann, and M. Hepting, **Unconventional crystal structure of the high-pressure superconductor  $\text{La}_3\text{Ni}_2\text{O}_7$**  (2023), [arXiv:2312.07341 \[cond-mat.supr-con\]](https://arxiv.org/abs/2312.07341).
- [23] H. Sakakibara, M. Ochi, H. Nagata, Y. Ueki, H. Sakurai, R. Matsumoto, K. Terashima, K. Hirose, H. Ohta, M. Kato, Y. Takano, and K. Kuroki, Theoretical analysis on the possibility of superconductivity in a trilayer Ruddlesden-Popper nickelate  $\text{La}_4\text{Ni}_3\text{O}_{10}$  under pressure and its experimental examination: comparison with  $\text{La}_3\text{Ni}_2\text{O}_7$  (2023), [arXiv:2309.09462](https://arxiv.org/abs/2309.09462).
- [24] Q. Li, Y.-J. Zhang, Z.-N. Xiang, Y. Zhang, X. Zhu, and H.-H. Wen, Signature of superconductivity in pressurized  $\text{La}_4\text{Ni}_3\text{O}_{10}$  (2023), [arXiv:2311.05453](https://arxiv.org/abs/2311.05453).
- [25] M. Zhang, C. Pei, X. Du, Y. Cao, Q. Wang, J. Wu, Y. Li, Y. Zhao, C. Li, W. Cao, S. Zhu, Q. Zhang, N. Yu, P. Cheng, J. Zhao, Y. Chen, H. Guo, L. Yang, and Y. Qi, Superconductivity in trilayer nickelate  $\text{La}_4\text{Ni}_3\text{O}_{10}$  under pressure (2023), [arXiv:2311.07423](https://arxiv.org/abs/2311.07423).
- [26] Y. Zhu, E. Zhang, B. Pan, X. Chen, L. Chen, H. Ren, F. Liu, J. Wang, D. Jia, H. Wo, Y. Gu, Y. Gu, L. Ji, W. Wang, H. Gou, Y. Shen, T. Ying, J. Guo, and J. Zhao, Signatures of superconductivity in trilayer  $\text{La}_4\text{Ni}_3\text{O}_{10}$  single crystals (2023), [arXiv:2311.07353](https://arxiv.org/abs/2311.07353).
- [27] J. Chaloupka and G. Khaliullin, Orbital Order and Possible Superconductivity in  $\text{LaNiO}_3/\text{LaMO}_3$  Superlattices, *Phys. Rev. Lett.* **100**, 016404 (2008).
- [28] P. Hansmann, X. Yang, A. Toschi, G. Khaliullin, O. K. Andersen, and K. Held, Turning a Nickelate Fermi Surface into a Cupratelike One through Heterostructuring, *Phys. Rev. Lett.* **103**, 016401 (2009).
- [29] A. V. Boris, Y. Matiks, E. Benckiser, A. Frano, P. Popovich, V. Hinkov, P. Wochner, M. Castro-Colin, E. Detemple, V. K. Malik, C. Bernhard, T. Prokscha, A. Suter, Z. Salman, E. Morenzoni, G. Cristiani, H.-U. Habermeier, and B. Keimer, Dimensionality Control of Electronic Phase Transitions in Nickel-Oxide Superlattices, *Science* **332**, 937 (2011).
- [30] M. Uchida, Y. Yamasaki, Y. Kaneko, K. Ishizaka, J. Okamoto, H. Nakao, Y. Murakami, and Y. Tokura, Pseudogap-related charge dynamics in the layered nickelate  $R_{2-x}\text{Sr}_x\text{NiO}_4$  ( $x \sim 1$ ), *Phys. Rev. B* **86**, 165126 (2012).
- [31] M. Uchida, K. Ishizaka, P. Hansmann, X. Yang, M. Sakano, J. Miyawaki, R. Arita, Y. Kaneko, Y. Takata, M. Oura, A. Toschi, K. Held, A. Chainani, O. K. Andersen, S. Shin, and Y. Tokura, Orbital characters of three-dimensional Fermi surfaces in  $\text{Eu}_{2-x}\text{Sr}_x\text{NiO}_4$  as probed by soft-x-ray angle-resolved photoemission spectroscopy, *Phys. Rev. B* **84**, 241109 (2011).
- [32] M. Uchida, K. Ishizaka, P. Hansmann, Y. Kaneko, Y. Ishida, X. Yang, R. Kumai, A. Toschi, Y. Onose, R. Arita, K. Held, O. K. Andersen, S. Shin, and Y. Tokura, Pseudogap of Metallic Layered Nickelate  $R_{2-x}\text{Sr}_x\text{NiO}_4$  ( $R = \text{Nd, Eu}$ ) Crystals Measured Using Angle-Resolved Photoemission Spectroscopy, *Phys. Rev. Lett.* **106**, 027001 (2011).
- [33] I. M. Kharlamova, L. V. Makhnach, A. E. Usenka, A. S. Lyakhov, L. S. Ivashkevich, and V. V. Pankov, Ruddlesden-popper phases  $\text{Sr}_3\text{Ni}_{2-x}\text{Al}_x\text{O}_{7-\delta}$  and some doped derivatives: Synthesis, oxygen nonstoichiometry and electrical properties, *Solid State Ionics* **324**, 241 (2018).
- [34] M. Zinkevich, Constitution of the sr-ni-o system, *Journal of Solid State Chemistry* **178**, 2818 (2005).
- [35] Q. Qin and Y.-f. Yang, High- $T_c$  superconductivity by mobilizing local spin singlets and possible route to higher  $T_c$  in pressurized  $\text{La}_3\text{Ni}_2\text{O}_7$ , *Phys. Rev. B* **108**, L140504 (2023).
- [36] Y.-f. Yang, G.-M. Zhang, and F.-C. Zhang, Interlayer valence bonds and two-component theory for high- $T_c$  superconductivity of  $\text{La}_3\text{Ni}_2\text{O}_7$  under pressure, *Phys. Rev. B* **108**, L201108 (2023).
- [37] W. Wú, Z. Luo, D.-X. Yao, and M. Wang, Charge Transfer and Zhang-Rice Singlet Bands in the Nickelate Superconductor  $\text{La}_3\text{Ni}_2\text{O}_7$  under Pressure (2023), [arXiv:2307.05662](https://arxiv.org/abs/2307.05662).
- [38] Z. Luo, X. Hu, M. Wang, W. Wú, and D.-X. Yao, Bilayer Two-Orbital Model of  $\text{La}_3\text{Ni}_2\text{O}_7$  under Pressure, *Phys. Rev. Lett.* **131**, 126001 (2023).
- [39] V. Christiansson, F. Petocchi, and P. Werner, Correlated Electronic Structure of  $\text{La}_3\text{Ni}_2\text{O}_7$  under Pressure, *Phys. Rev. Lett.* **131**, 206501 (2023).
- [40] F. Lechermann, J. Gondolf, S. Bötzel, and I. M. Eremin, Electronic correlations and superconducting instability in  $\text{La}_3\text{Ni}_2\text{O}_7$  under high pressure, *Phys. Rev. B* **108**, L201121 (2023).
- [41] M. Nakata, D. Ogura, H. Usui, and K. Kuroki, Finite-energy spin fluctuations as a pairing glue in systems with coexisting electron and hole bands, *Phys. Rev. B* **95**, 214509 (2017).
- [42] Y. Gu, C. Le, Z. Yang, X. Wu, and J. Hu, Effective model and pairing tendency in bilayer Ni-based superconductor  $\text{La}_3\text{Ni}_2\text{O}_7$  (2023), [arXiv:2306.07275](https://arxiv.org/abs/2306.07275).
- [43] X. Chen, P. Jiang, J. Li, Z. Zhong, and Y. Lu, Critical charge and spin instabilities in superconducting  $\text{La}_3\text{Ni}_2\text{O}_7$  (2023), [arXiv:2307.07154](https://arxiv.org/abs/2307.07154).
- [44] D. A. Shilenko and I. V. Leonov, Correlated electronic structure, orbital-selective behavior, and magnetic correlations in double-layer  $\text{La}_3\text{Ni}_2\text{O}_7$  under pressure, *Phys. Rev. B* **108**, 125105 (2023).
- [45] C. Lu, Z. Pan, F. Yang, and C. Wu, Interplay of two Eg orbitals in Superconducting  $\text{La}_3\text{Ni}_2\text{O}_7$  Under Pressure (2023), [arXiv:2310.02915](https://arxiv.org/abs/2310.02915).

- [46] Y. Zhang, L.-F. Lin, A. Moreo, and E. Dagotto, Electronic structure, dimer physics, orbital-selective behavior, and magnetic tendencies in the bilayer nickelate superconductor  $\text{La}_3\text{Ni}_2\text{O}_7$  under pressure, *Phys. Rev. B* **108**, L180510 (2023).
- [47] H. Oh and Y.-H. Zhang, Type-II  $t-J$  model and shared superexchange coupling from Hund's rule in superconducting  $\text{La}_3\text{Ni}_2\text{O}_7$ , *Phys. Rev. B* **108**, 174511 (2023).
- [48] H. Lange, L. Homeier, E. Demler, U. Schollwöck, F. Grusdt, and A. Bohrdt, Feshbach resonance in a strongly repulsive bilayer model: a possible scenario for bilayer nickelate superconductors (2023), [arXiv:2309.15843](https://arxiv.org/abs/2309.15843).
- [49] M. Bianchini, A. Schiele, S. Schweidler, S. Sicolo, F. Fauth, E. Suard, S. Indris, A. Mazilkin, P. Nagel, S. Schuppler, M. Merz, P. Hartmann, T. Brezesinski, and J. Janek, From  $\text{LiNiO}_2$  to  $\text{Li}_2\text{NiO}_3$ : Synthesis, structures and electrochemical mechanisms in Li-rich nickel oxides, *Chemistry of Materials* **32**, 9211 (2020).
- [50] T. Ohnuma and T. Kobayashi, X-ray absorption near edge structure simulation of  $\text{LiNi}_0.5\text{Co}_0.2\text{Mn}_0.3\text{O}_2$  via first-principles calculation, *RSC Advances* **9**, 35655 (2019).
- [51] B. Beznosikov and K. Aleksandrov, Perovskite-like crystals of the ruddlesden-popper series, *Crystallography Reports* **45**, 792 (2000).
- [52] P. Puphal, V. Sundaramurthy, V. Zimmermann, K. Küster, U. Starke, M. Isobe, B. Keimer, and M. Hepting, Phase formation in hole- and electron-doped rare-earth nickelate single crystals, *APL Materials* **11** (2023).
- [53] P. Puphal, Y.-M. Wu, K. Fürsich, H. Lee, M. Pakdaman, J. A. N. Bruin, J. Nuss, Y. E. Suyolcu, P. A. van Aken, B. Keimer, M. Isobe, and M. Hepting, Topotactic transformation of single crystals: From perovskite to infinite-layer nickelates, *Sci. Adv.* **7**, eabl8091 (2021).
- [54] P. Puphal, B. Wehinger, J. Nuss, K. Küster, U. Starke, G. Garbarino, B. Keimer, M. Isobe, and M. Hepting, Synthesis and physical properties of  $\text{LaNiO}_2$  crystals, *Phys. Rev. Mater.* **7**, 014804 (2023).
- [55] Z. Liu, H. Sun, M. Huo, X. Ma, Y. Ji, E. Yi, L. Li, H. Liu, J. Yu, Z. Zhang, Z. Chen, F. Liang, H. Dong, H. Guo, D. Zhong, B. Shen, S. Li, and M. Wang, Evidence for charge and spin density waves in single crystals of  $\text{La}_3\text{Ni}_2\text{O}_7$  and  $\text{La}_3\text{Ni}_2\text{O}_6$ , *Sci. China Phys. Mech. Astron.* **66**, 217411 (2022).
- [56] X. Wang, K. Huang, L. Yuan, S. Xi, W. Yan, Z. Geng, Y. Cong, Y. Sun, H. Tan, X. Wu, L. Li, and S. Feng, Activation of surface oxygen sites in a cobalt-based perovskite model catalyst for CO oxidation, *J. Phys. Chem. Lett.* **9**, 4146 (2018).
- [57] A. Abragam and B. Bleaney, *Electron paramagnetic resonance of transition ions*, Dover books on physics and chemistry (Dover Publ., New York, N. Y., 1986) unabridged and corrected republication of the work first published by the Clarendon Press (Oxford University Press) in 1970 in the International series of monographs on physics—T.p. verso.
- [58] M. C. Biesinger, Accessing the robustness of adventitious carbon for charge referencing (correction) purposes in xps analysis: Insights from a multi-user facility data review, *Applied Surface Science* **597**, 153681 (2022).